Bioactive Materials 47 (2025) 51–63

Contents lists available at ScienceDirect

Bioactive Materials

journal homepage: www.keaipublishing.com/en/journals/bioactive-materials

Self-healable and pH-responsive spermidine/ferrous ion complexed hydrogel Co-loaded with CA inhibitor and glucose oxidase for combined cancer immunotherapy through triple ferroptosis mechanism

Tianqi Nie [a,1], Yifei Fang [b,c,1], Ruhe Zhang [d], Yishui Cai [b], Xiaobo Wang [d,**], Yuenong Jiao [a,***], Jun Wu [b,c,d,*]

[a] Department of Otorhinolaryngology Head and Neck Surgery, Guangzhou Twelfth People's Hospital (The Affiliated Twelfth People's Hospital of Guangzhou Medical University), Guangzhou Medical University, Guangzhou, 510620, China
[b] Bioscience and Biomedical Engineering Thrust, The Hong Kong University of Science and Technology (Guangzhou), Guangzhou, 511400, China
[c] Division of Life Science, The Hong Kong University of Science and Technology, Hong Kong, China
[d] Department of Hematology, The Seventh Affiliated Hospital of Sun Yat-sen University, Shenzhen, 518106, China

ARTICLE INFO

Keywords:
Spermidine
Tumor metabolic reprogramming
Ferroptosis
Autophagy
Carbonic anhydrases

ABSTRACT

Tumor microenvironment governs various therapeutic tolerability of cancer such as ferroptosis and immunotherapy through rewiring tumor metabolic reprogramming like Warburg metabolism. Highly expressed carbonic anhydrases (CA) in tumor that maintaining the delicate metabolic homeostasis is thus the most potential target to be modulated to resolve the therapeutic tolerability. Hence, in this article, a self-healable and pH-responsive spermidine/ferrous ion hydrogel loaded with CA inhibitor (acetazolamide, ACZ) and glucose oxidase (ACZ/GOx@SPM-HA Gel) was fabricated through the Schiff-base reaction between spermidine-dextran and oxidized hyaluronic acid, along with ferrous coordination. Investigation on cancer cell lines (MOC-1) demonstrated ACZ/GOx@SPM-HA Gel may induce cellular oxidative stress and mitochondrial dysfunction through disrupting the cellular homeostasis. Moreover, with the facilitation of autophagy induced by spermidine, ACZ/GOx@SPM-HA Gel may trigger a positive feedback loop to maximally amplify cellular ferroptosis and promote DAMPs release. The anti-tumor evaluation on xenograft mice models furtherly proved the local injection of such hydrogel formulation could efficiently inhibit the tumor growth and distinctively promote the immunogenicity of tumor bed to provide a more favorable environment for immunotherapy. Overall, ACZ/GOx@SPM-HA Gel, with such feasible physiochemical properties and great biocompatibility, holds great potential in treating solid tumors with acidosis-mediated immunotherapy tolerance.

1. Introduction

Despite the conventional treatment strategies like surgery or radiotherapy, the field of immunotherapy for cancer treatment has witnessed significant advancements in the past few years [1–3]. To date, the U.S. Food & Drug Administration (FDA) has now approved various immune checkpoint inhibitors such as Nivolumab, Pembrolizumab, Atezolizumab, Ipilimumab for cancer immunotherapy ranging from melanoma and non-small-cell lung cancer to advanced cutaneous squamous cell carcinoma [4,5]. However, owing to overall low response rate (5–30 %) and the immune-related adverse events (irAEs) such as colitis, its further application for cancer treatment is still confined before more clinical trials and evaluations [6–8]. Recently, ferroptosis as a type of non-apoptotic cell death has emerged as a synergistic candidate to enhance the tumor vulnerability and susceptibility to immunotherapy through triggering the release of DAMPs (damage-associated molecular patterns)

* Corresponding author. Bioscience and Biomedical Engineering Thrust, The Hong Kong University of Science and Technology (Guangzhou), No.1 Du Xue Road, Nansha, Guangzhou, 511400, China.
** Corresponding author. Department of Hematology, The Seventh Affiliated Hospital of Sun Yat-sen University, 628 Zhenyuan Road, Xinhu Street, Guangming, Shenzhen, 518106, China.
*** Corresponding author. Department of Otorhinolaryngology Head and Neck Surgery, Guangzhou Twelfth People's Hospital, Guangzhou, 510620, China.
E-mail addresses: wangxiaobo@sysush.com (X. Wang), jyl606@139.com (Y. Jiao), junwuhkust@ust.hk (J. Wu).
[1] These authors contributed equally in this work.

https://doi.org/10.1016/j.bioactmat.2025.01.005
Received 1 July 2024; Received in revised form 24 December 2024; Accepted 7 January 2025

[9–11]. Nevertheless, metabolic status like acidosis or hypoxia, and redox homeostasis modulated by cysteine/glutathione (GSH)/glutathione peroxidase 4 (GPX4) axis would also increase the ferroptosis tolerability in cancer [12–15]. Therefore, interference of cellular metabolic homeostasis would be a fascinating strategy to maximally amplify the ferroptosis in tumor tissues and effectively improve the immunotherapy outcomes in clinical cancer treatments.

With the aggressive impetus to investigate cancer metabolism recently, tumor acidosis has proven to be another critical hallmark of tumor microenvironment (TME) [16,17]. Generally, tumor acidosis is originally derived from low partial pressure of oxygen [18]. Specifically, limited oxygen diffusion and consumption in tumors may initiate a shift in carbon utilization, leading to a reliance on glycolysis instead of oxidative phosphorylation for energy production [19]. Consequently, this metabolic reprogramming, widely known as Warburg metabolism, would lead to the massive accumulation of acidic by-products *e.g.,* lactic acid, and ultimately result to tumor acidosis, which is devastating for the proliferation of cancer cells [20–23]. pH regulatory enzymes thus are key mediators for cancer cells to maintain the tumor pH homeostasis. Carbonic anhydrases (CA) are a type of metalloenzymes that may reversibly catalyze the hydration of CO_2 to HCO_3^- and protons, which is crucial for maintaining the delicate balance between extracellular and intracellular pH [24,25]. Owing to this, CA as a cell surface and extracellular facing enzyme, is highly expressed in various cancer cells to orchestrate invasion and metastasis, thus has proved as an indicator to predict the poor prognosis in several solid tumors [26–28]. Moreover, CA -mediated tumor pH homeostasis is also devasting to T cell response as excessive acidic by-products may inhibit the glycolytic pathway of T cell and impair its proliferation and cytokine production through abrogating the lactate concentration gradient across T cell membrane [29,30]. Additionally, through a synthetic CRISPR lethal screen, Shoukat Dedhar et al. firstly unveiled and identified CA IX-NFS1/xCT axis as a potential target to overcome acidosis-mediated ferroptosis tolerability and other therapeutic resistance, which underlines the significance of CA IX as a critical target to disrupt the tumor pH homeostasis and improve the ferroptosis/immunotherapy tolerability in tumors [31].

Autophagy, as a conserved self-degradative process, is another key regulator in maintenance of cellular metabolic homeostasis, which could promote tumor progression and increase chemotherapy resistance in specific cases [32–34]. Intriguingly, recent studies have indicated the intimate interplay between autophagy and ferroptosis [35,36]. Under certain circumstances, autophagy is considered as a reinforcer that enhance ROS-dependent ferroptosis via disrupting redox homeostasis. Specifically, Autophagy triggered by excessive reactive oxygen species (ROS) and lipid peroxidation (LPO) derived from ferroptosis can further promote iron and ROS accumulation, which may form a positive feedback loop to continuously amplify the ferroptosis [37–39]. The rationale to cascade amplifies on ferroptosis in cancer cells through autophagy is thus highly feasible. In fact. Zheng et al. has verified such speculation in their research, demonstrating the autophagy depletion in HSC-LX2 cells would increase the accumulation of oxidized lipids and enhance their tolerability to ferroptosis [40]. Moreover, Wu et al. introduced spermidine, an autophagy inducer, to prepare a self-assembly metal--immunopeptide nanocomplexes for enhancing ferroptosis vulnerability of lymphomas, and thus synergistically improve the immunotherapy efficacy of lymphoma [41]. Overall, facilitated by autophagy as a further reinforcer of ferroptosis, interference with cellular pH and redox homeostasis emerges as a potential strategy to enhance ferroptosis vulnerability and maximally improve the immunotherapy of HNC [42,43].

Hence, in this article, a self-healable and pH-responsive spermidine hydrogel loaded with CA inhibitor (acetazolamide, ACZ) and GOx was fabricated through the Schiff-base reaction between spermidine-dextran (SPM-DEX) and oxidized hyaluronic acid (HA-ALD), and the metal ions (Fe^{2+}) coordination as indicated in Scheme 1. Its effect on disrupting the pH and redox homeostasis was firstly demonstrated on cancer cell lines (MOC-1).Moreover, the mechanism being facilitated with autophagy to maximally amplify the ferroptosis in MOC-1 cells was also elucidated.

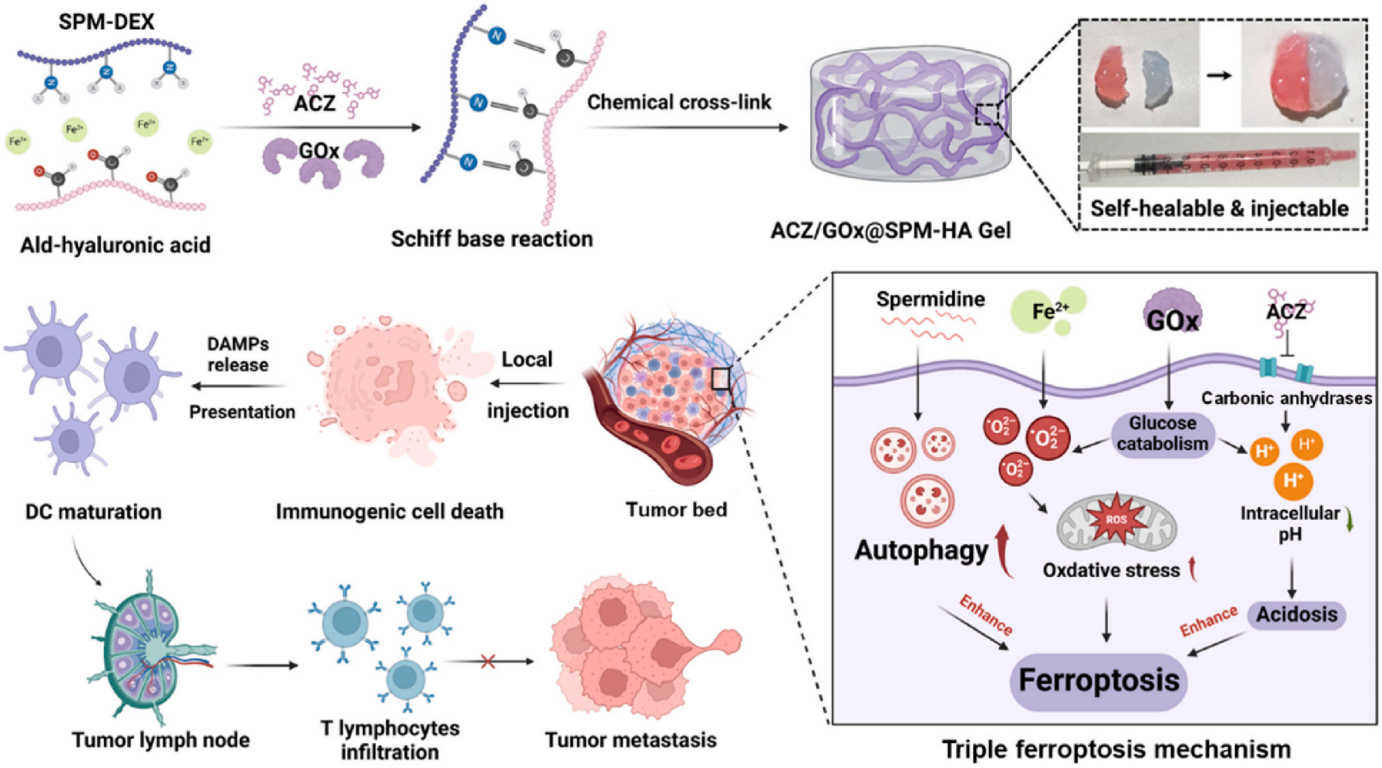

Scheme 1. (A) Synthesis of ACZ/GOx@SPM-HA Gel via Schiff-base reaction between SPM-DEX and HA-ALD. (B) Schematic illustration of the antitumor mechanism of ACZ/GOx@SPM-HA Gel through autophagy-dependent ferroptosis.

The anti-tumor efficacy and anti-metastatic efficacy combing with anti-PD-L1 were further investigated on MOC-1 xenograft mice model and metastasis mice model. Overall, ACZ/GOx@SPM-HA Gel holds significant potential in treating solid tumors with acidosis-mediated immunotherapy tolerance.

2. Materials and methods

2.1. Animal study

C57BL/6 mice used in this research were purchased from Guangdong Medical Laboratory Animal Center (Guangzhou, China). All experiments were performed in accordance with a protocol approved by the Institutional Animal Care and Use Committee of Sun Yat-sen University (SYSU-IACUC-2023-000577).

2.2. Preparation and characterization of ACZ/GOx@SPM-HA Gel

The spermidine hydrogel was prepared based on the Schiff-base reaction between SPM-DEX and HA-ALD. In specific, stock solution of each component was prepared in advance (100 mg/mL SPM-DEX, 100 mg/mL HA-ALD, 2 mg/mL $FeSO_4$, 160 mg/mL ACZ, and 2 mg/mL GOx). After that, SPM-HA hydrogel without Fe^{2+} was prepared by simple mixture of SPM-DEX and HA-ALD at volume ratio of 1:1 (V/V). The other formulations including SPM-HA Gel, ACZ@SPM-HA Gel, GOx@SPM-HA Gel, and ACZ/GOx@SPM-HA Gel were prepared according to the above protocol with corresponding components to be dispersed in HA-ALD priorly. The final content of each component was as follows: 50 mg/mL SPM-DEX, 50 mg/mL HA-ALD, 0.2 mg/mL $FeSO_4$, 1.6 mg/mL ACZ, and 0.1 mg/mL GOx. The morphology and structure of as prepared hydrogel were characterized by scanning electron microscope (SEM) and FT-IR. Basic physiochemical properties including swelling ratio, self-healing, mechanical properties, hemocompatibility, release kinetics were also evaluated. The catabolism of GOx on glucose oxidation was also tested through Hydrogen Peroxide Assay Kit purchased from Beyotime Institute of Biotechnology (Haimen, China) in the presence of 20 mM glucose.

Swelling ratio of ACZ/GOx@SPM-HA Gel. The swelling ratio of ACZ/GOx@SPM-HA were further evaluated according to our previous protocol. Briefly, SPM-HA Gel and ACZ/GOx@SPM-HA were prepared according to the aforementioned procedures followed with lyophilization. Their original weights were weighed and recorded as W_0. After that, these two hydrogels were immersed into PBS buffer and their weights were weighed every 20 min and recorded as W_t. The swelling ratio of ACZ/GOx@SPM-HA at a specific time interval was then expressed as the percentage of W_0.

Hemocompatibility of ACZ/GOx@SPM-HA Gel. Blood samples anticoagulated with heparin sodium (12 IU/mL) were collected from C57BL/6 mice. The blood cells were centrifuged, then washed with saline buffer for three times following with suspension in saline buffer at a content of 4 % (v/v). After that, SPM-HA Gel and ACZ/Gox@SPM-HA Gel were incubated in saline buffer to obtain the extracts. Four groups were set in the experiment: (1) Negative Control: 1 mL saline buffer + 1 mL blood cells suspension; (2) SPM-HA Gel: 1 mL SPM -HA Gel extract + 1 mL blood cells suspension; (3) ACZ/GOx@SPM-HA Gel: 1 mL ACZ/GOx@SPM-HA extract + 1 mL blood cells suspension; (4) Positive Control: 1 mL deionized water + 1 mL blood cells suspension. All the groups were incubated for 2 h at 37 °C. Finally, supernatant from each group was collected and the absorbance was determined by microplate reader at 540 nm.

2.3. In vivo antitumor efficacy of ACZ/GOx@SPM-HA Gel

MOC-1 tumor-bearing mice models were used to evaluate the antitumor efficacy of ACZ/Gox@SPM-HA Gel. Briefly, C57BL/6 mice were subcutaneously injected with 1×10^6 MOC-1 cells at the right limb. Mice with tumor volume reaching ~150 mm^3 were chosen and randomly divided into 6 groups (5 mice per group) for the evaluation: (1) Control: intratumoral (*i.t.*) injection of 100 μL saline; (2)SPM-HA Gel without Fe^{2+}: *i.t.* injection of 100 μL SPM-HA Gel without Fe^{2+}; (3) SPM-HA Gel: *i.t.* injection of 100 μL SPM-HA Gel (1 mg/kg Fe^{2+}); (4) ACZ@SPM-HA Gel: *i.t.* injection of 100 μL ACZ@SPM-HA Gel (1 mg/kg Fe^{2+}, 8 mg/kg ACZ); (5) GOx@SPM-HA Gel: *i.t.* injection of 100 μL GOx@SPM-HA Gel (1 mg/kg Fe^{2+}, 0.5 mg/kg GOx); (6) ACZ/GOx@SPM-HA Gel: *i.t.* injection of 100 μL ACZ/GOx@SPM-HA Gel (1 mg/kg Fe^{2+}, 8 mg/kg ACZ and 0.5 mg/kg GOx). Tumor volume from each treatment group was measured by caliper with the length (L) and width (W), then calculated based on the following equation: $0.5 \times L \times W^2$ (mm^3). The whole evaluation lasted for 12 days, during which mice body weight and tumor volume were recorded every other day. After that, mice were euthanized, major organs and tumors were resected for further histological analysis (Ki67, TUNEL, and CRT) and ELISA essay of cytokines including TNF-α, IL-6, and IFN-γ.

2.4. Combinative antitumor efficacy of ACZ/GOx@SPM-HA Gel with anti-PD-L1

MOC-1 tumor-bearing mice metastatic models were used to evaluate the combinative antitumor efficacy of ACZ/GOx@SPM-HA Gel with Anti-PD-L1. Briefly, C57BL/6 mice were firstly subcutaneously injected with 1×10^6 MOC-1 cells at the right limb. After four days, left limb of mice were also subcutaneously injected with 1×10^6 MOC-1 cells. Mice with tumor volume on right limb reaching ~150 mm^3 were chosen and randomly divided into 4 groups (5 mice per group) for the evaluation: (1) Control: *i.t.* injection of 100 μL saline at primary tumor; (2) ACZ/GOx@SPM-HA Gel: *i.t.* injection of 100 μL ACZ/GOx@SPM-HA Gel at primary tumor (1 mg/kg Fe^{2+}, 8 mg/kg ACZ and 0.5 mg/kg GOx); (3) Anti-PD-L1: *i.t.* injection of 100 μL Anti-PD-L1 solution at primary tumor (5 mg/kg; 2 dosages); (4) Gel + Anti-PD-L1: *i.t.* injection of 100 μL ACZ/GOx@SPM-HA Gel (1 mg/kg Fe^{2+}, 8 mg/kg ACZ and 0.5 mg/kg GOx) and 100 μL Anti-PD-L1 solution at primary tumor (5 mg/kg; 2 dosages). Tumor volume from each treatment group was measured by caliper with the length (L) and width (W), then calculated based on the following equation: $0.5 \times L \times W^2$ (mm^3). The whole evaluation lasted for 14 days, during which mice body weight and tumor volume on both limbs were recorded every other day, different formulations were administered on Day 0 and 7. After that, mice blood samples were collected for ELISA essay of cytokines including TNF-α, IL-6, and IFN-γ, and then euthanized, tumors were resected for further histological analysis (Ki67, TUNEL, CD31) and lymphocyte infiltration detection.

2.5. Statistical analysis

All values are expressed as mean ± standard deviation (SD). Comparisons among all groups were evaluated using one-way analysis of variance or Student's *t*-test using GraphPad Prism version 9.0 for Windows (GraphPad Software, USA), and $p < 0.05$, $p < 0.01$, $p < 0.001$, or $p < 0.0001$ were considered statistically significant.

3. Results and discussion

3.1. Preparation and characterization of ACZ/GOx@SPM-HA Gel

SPM-DEX and HA-ALD were initially synthesized as described in supplementary information (Section 1.2) and the structure was verified by ^1H NMR (Fig. S1). Spermidine hydrogel (SPM-HA Gel) was then prepared through Schiff-base reaction between SPM-DEX and HA-ALD as depicted in Fig. 1A. SPM-HA Gel loaded with ACZ and GOx (ACZ/GOx@SPM-HA Gel) was prepared through similar procedures as indicated in Materials and Methods. The production of H_2O_2 by GOx-catalyzed glucose oxidation was then tested through Hydrogen Peroxide Assay Kit. As indicated in Fig. S2, the increasement of H_2O_2

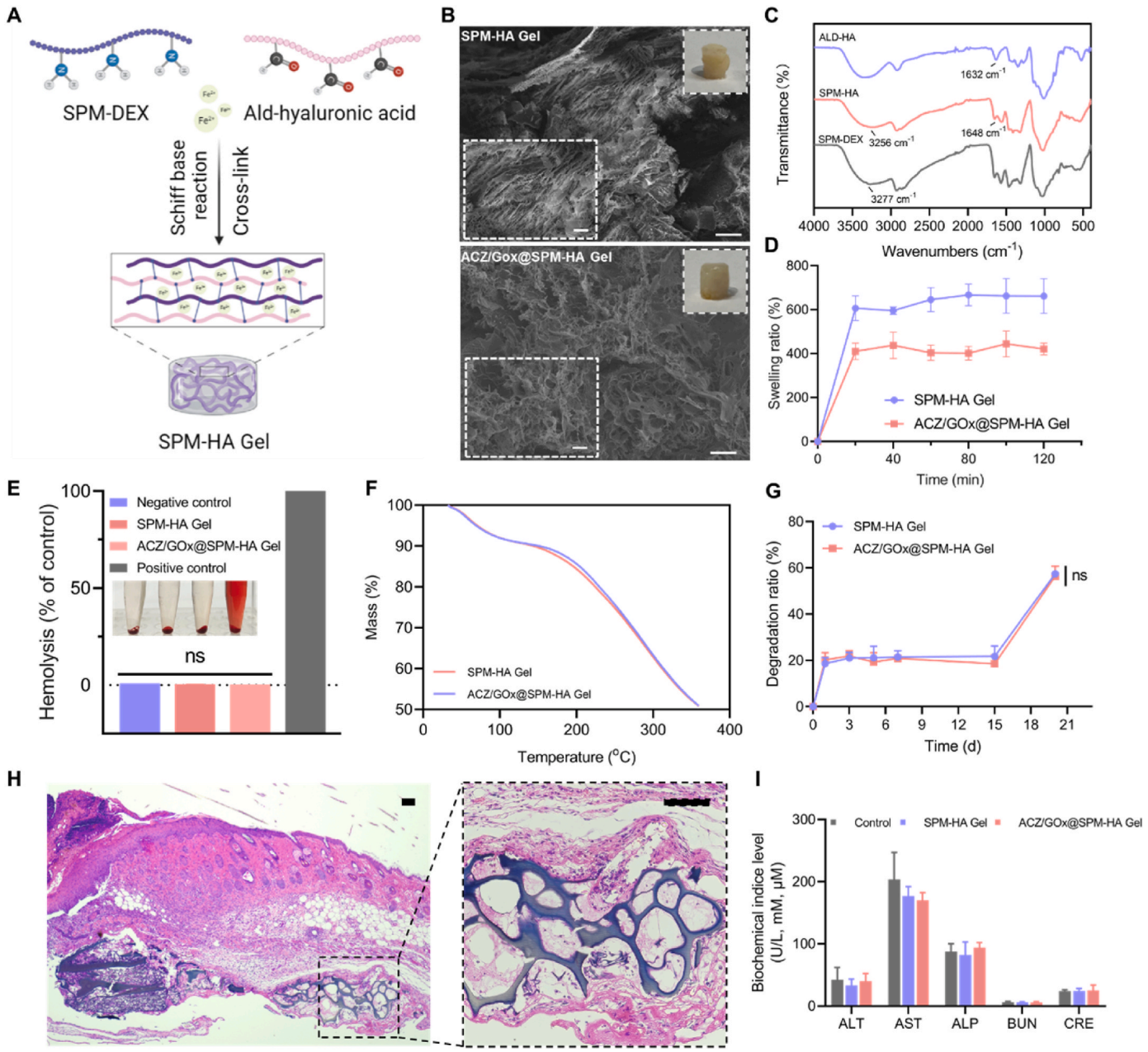

Fig. 1. Preparation and characterization of ACZ/GOx@SPM-HA Gel. (A) SPM-HA Gel was prepared through the Schiff-base reaction between SPM-DEX and HA-ALD. (B) Morphological study of SPM-HA Gel and ACZ/GOx@SPM-HA Gel by SEM, scale bar = 100 μm (inset scale bar = 20 μm). (C) FT-IR spectrum of SPM-HA Gel. (D) Swelling ratio, (E) Hemocompatibility, (F) Thermogravimetric analysis, and (G) *In vitro* degradation of ACZ/GOx@SPM-HA Gel. (H) *In vivo* degradation of ACZ/GOx@SPM-HA Gel after subcutaneous injection in mice, scale bar = 100 μm. (I) Biochemical indices of mice after subcutaneous injection of ACZ/GOx@SPM-HA Gel for 12 days, ALT: alanine aminotransferase; AST: aspartate transaminase; ALP: alkaline phosphatase; BUN: blood urea nitrogen; CRE: creatinine. All data are shown as mean ± SD (n = 3).

level was highly correlated with the time and the GOx concentration, demonstrating the glucose oxidation catalyzed by GOx and its potential in disturbing the cellular redox homeostasis. After that, morphology of SPM-HA Gel and ACZ/GOx@SPM-HA Gel was studied by SEM. As indicated in Fig. 1B, a distinct and regular 3D porous structure of SPM-HA Gel could be observed with pore size at ~5 μm, suggesting the successful cross-linking between SPM-DEX and HA-ALD through Schiff-base reaction. Besides that, though loading with ACZ and GOx, the porous structure of ACZ/GOx@SPM-HA Gel was still maintained only with pore size enlarged to ~10 μm. The chemical cross-linking between SPM-DEX and HA-ALD was also confirmed through FT-IR. As shown in Fig. 1C, the stretching vibration peak (~3277 cm^{-1}) of amine group in the spectrum of SPM-DEX redshifted to ~ 3256 cm^{-1} in the spectrum of SPM-HA, indicating the molecular interaction between SPM-DEX and HA-ALD. Correspondingly, a new absorption peak at ~1648 cm^{-1}, representative peak of imine group (-C=N), was detected in the spectrum of SPM-HA, further verifying the Schiff-base reaction between these two components. Besides, the disappearance of absorption peak at ~1632 cm^{-1} derived from aldehyde group in the spectrum of SPM-HA also supported the conclusion above.

After confirming the successful preparation, the physiochemical properties of ACZ/Gox@SPM-HA Gel were characterized. As indicated in Fig. 1D, the swelling ratio of SPM-HA Gel could be high up to ~600 % in 20 min and maintained at this level in the following 2 h. Besides, the laden drugs did not alter the swelling ratio (~400 %) significantly, which is crucial for the hygroscopicity and anchor of hydrogel

formulation in tissues after topical injection [44]. The hemolysis test (Fig. 1E) further confirmed the biosafety of ACZ/Gox@SPM-HA Gel *in vivo* as its hemolysis ratio was nearly closed to 0 %. Even after loading with ACZ and GOx, the hemolysis ratio did not change significantly, indicating the great hemocompatibility and the prevention of drug leakage fulfilled by the chemical cross-linking. Biodegradation of hydrogel formulations is another essential property for their clinical application and translation [45]. Therefore, the degradation and thermostability of each component in the hydrogel was preliminarily investigated by thermogravimetry (TG). As shown in Fig. 1F, both SPM-HA Gel and ACZ/GOx@SPM-HA Gel exhibited a similar declining trend in mass. Specifically, around 100 °C, the mass of both hydrogel formulations dropped for 10 % significantly due to the evaporation of water. With the enhancement of temperature (~200–300 °C), a 30 % mass was lost owing to the burning and decomposition of SPM-DEX, HA and the laden drugs. The degradation ratio was thus further investigated both *in vitro* and *in vivo* according to the protocols describe in Section 1.11 of supplementary information. As indicated in Fig. 1G and Fig. S3, the degradation ratio in the first 12 days maintained about 20–25 % with a higher ratio *in vivo* considering the catalysis of relative enzymes may accelerate the degradation process. To date, low molecular weight HA (LMW-HA) as an integral component of extracellular matrix (ECM) in tumor, plays critical role in tumor progression and metastasis. The high expression of hyaluronidases in various types of tumor tissues was thus often detected and reported [46]. Therefore, the degradation ratio of this polysaccharide-based hydrogel under enzymatic environment (0.04 U/mL hyaluronidases) was further evaluated. As observed in Fig. S4, the degradation ratio of both SPM-HA Gel and ACZ/GOx@SPM-HA Gel was significantly enhanced to ~70 % on Day 1 and then almost degraded completely after 7 days, demonstrating its great biodegradability. The epidermal slices through H&E staining (Fig. 1H) distinctively presented this process as the implanted hydrogel beneath the epidermis has decomposed into pieces (indicated as purple color) instead an intact mass after 12 days evaluation. Biochemical indices from each treatment group (Fig. 1I and Fig. S5) further proved additional evidence of the biocompatibility and low acute toxicity of ACZ/GOx@SPM-HA Gel as liver function indicators (ALT, AST, ALP) and kidney function indicators (BUN, CRE) were all comparable to the control healthy group on both 1 day and 12 day-post subcutaneous implantation. Besides, pathological changes or inflammation sites could hardly be observed in the major organ slices stained by H&E (Fig. S6), further confirming its histocompatibility. Taken together, ACZ/GOx@SPM-HA Gel with such feasible physiochemical properties and great hemocompatibility and histocompatibility would be suitable for the further investigation on animal evaluations.

As a chemical crosslinking hydrogel based on Schiff reaction, SPM-HA Gel may exhibit fascinating physiochemical properties under specific given environmental conditions. As indicated in Fig. 2A, the dynamic interaction between amine groups and aldehyde groups enables SPM-HA Gel to self-heal intactly within a very short time after cut. Moreover, thanks to its self-healing capability, SPM-HA Gel could still be injectable even after gelation, which ensure its further biomedical application and clinical translation. In specific, self-healing hydrogel is always injectable, which thus enables the direct injection of hydrogel formulations into tumor tissue while still maintain the tumor tissues in their natural state. Additionally, owing to its self-healing property, hydrogels may also preserve their pore structure and anchor in the tumor tissue to promote the uniform distribution of laden

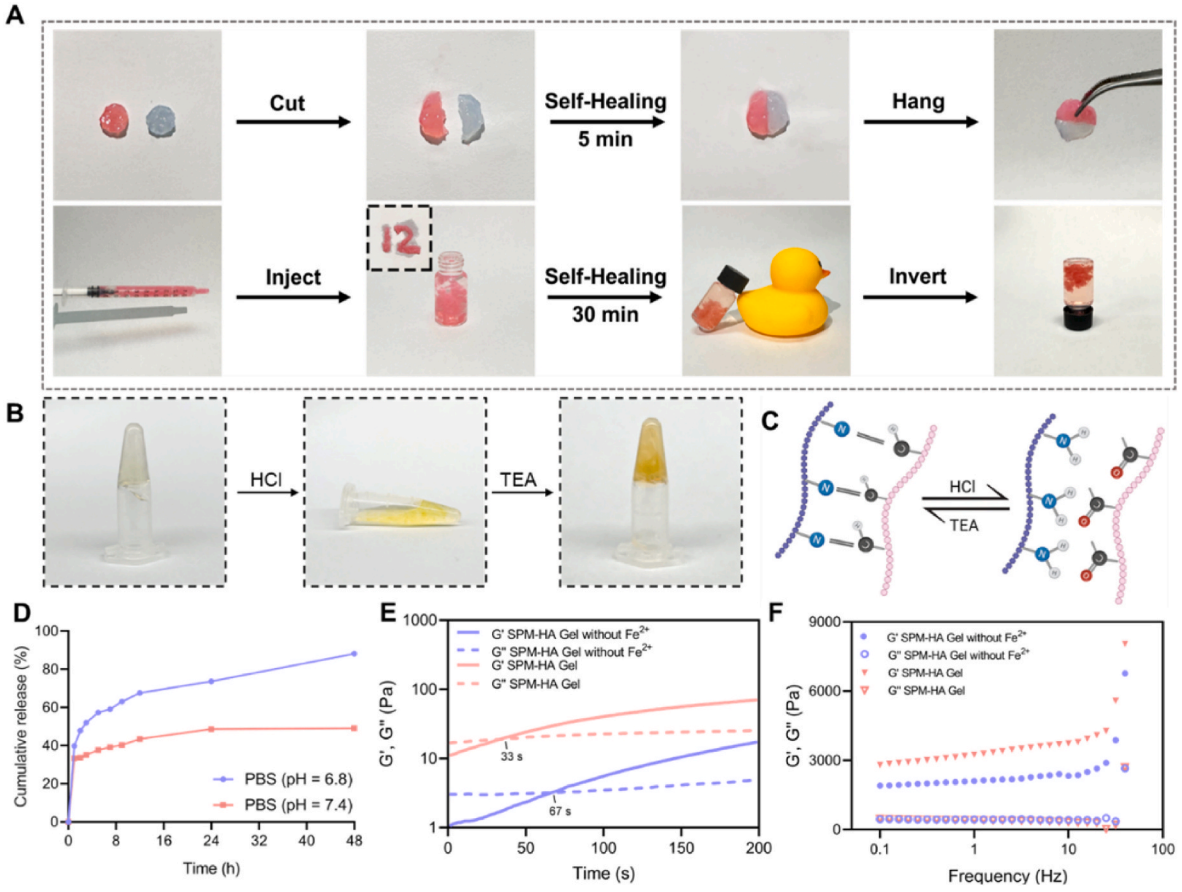

Fig. 2. Self-healing and controllable release kinetics based on dynamic chemical cross-linking. Representative photo of (A) self-healing property and (B) pH-responsive gelation of SPM-HA Gel. (C) Schematic illustration of pH-responsive gelation based on Schiff-base reaction. (D) *In vitro* release profile of SPM-HA Gel under different pH. (E) Gelation time, and (F) Viscoelasticity of SPM-HA Gel.

chemotherapeutics [47,48]. For the syringe needle size, considering the condense chemical cross-linking between SPM-DEX and oxidized HA, 26G syringe needle size (0.45 mm) or even larger size (18G-24G) would be more applicable for the injection of ACZ/GOx@SPM-HA Gel in cancer treatment [49]. To date, Schiff reaction may be reverted when amine groups are protonated. Therefore, the gelation between SPM-DEX and HA-ALD under different pH was studied. As observed in Fig. 2B and 2C, owing to the protonation of SPM-DEX, SPM-HA Gel could dissociate and turn back into fluid under acidic environment. Moreover, this process could be reverted after the pH environment was adjusted back to alkaline. Considering its pH-responsive gelation property, the release kinetic of laden drugs was thus further investigated based on the protocols described in Supplementary information (Section 1.3). It could be noted in Fig. 2D, under alkaline environment (pH = 7.4), the cumulative release of Fe^{2+} could only be ~40 % in the first 12 h and maximally plateaued to ~50 % in 48 h. In contrast, under weak acidic environment, the cumulative release of Fe^{2+} in the first 12 h could be high up to ~70 % and maximally plateaued to ~90 % in 48 h, exhibiting a pH-responsive release kinetics. Besides that, the release of laden ACZ and GOx (Figs. S7A–S7B) also exhibited a similar pH-responsive behavior under alkaline or acidic environment, which was consistent with pH-responsive gelation property of SPM-HA Gel. Mechanistically, under acidic environment, the amine group of SPM-DEX in the gel would be pronated and its dynamic Schiff base reaction with oxidized HA would weaken, thereby the cross-linking of the gel formulation would loose and thus release more laden component into the ambient environment.

In addition to the dynamic interaction between amine groups and aldehyde groups, metal ions coordination in the hydrogel scaffold also plays a critical role in its physiochemical properties particularly its

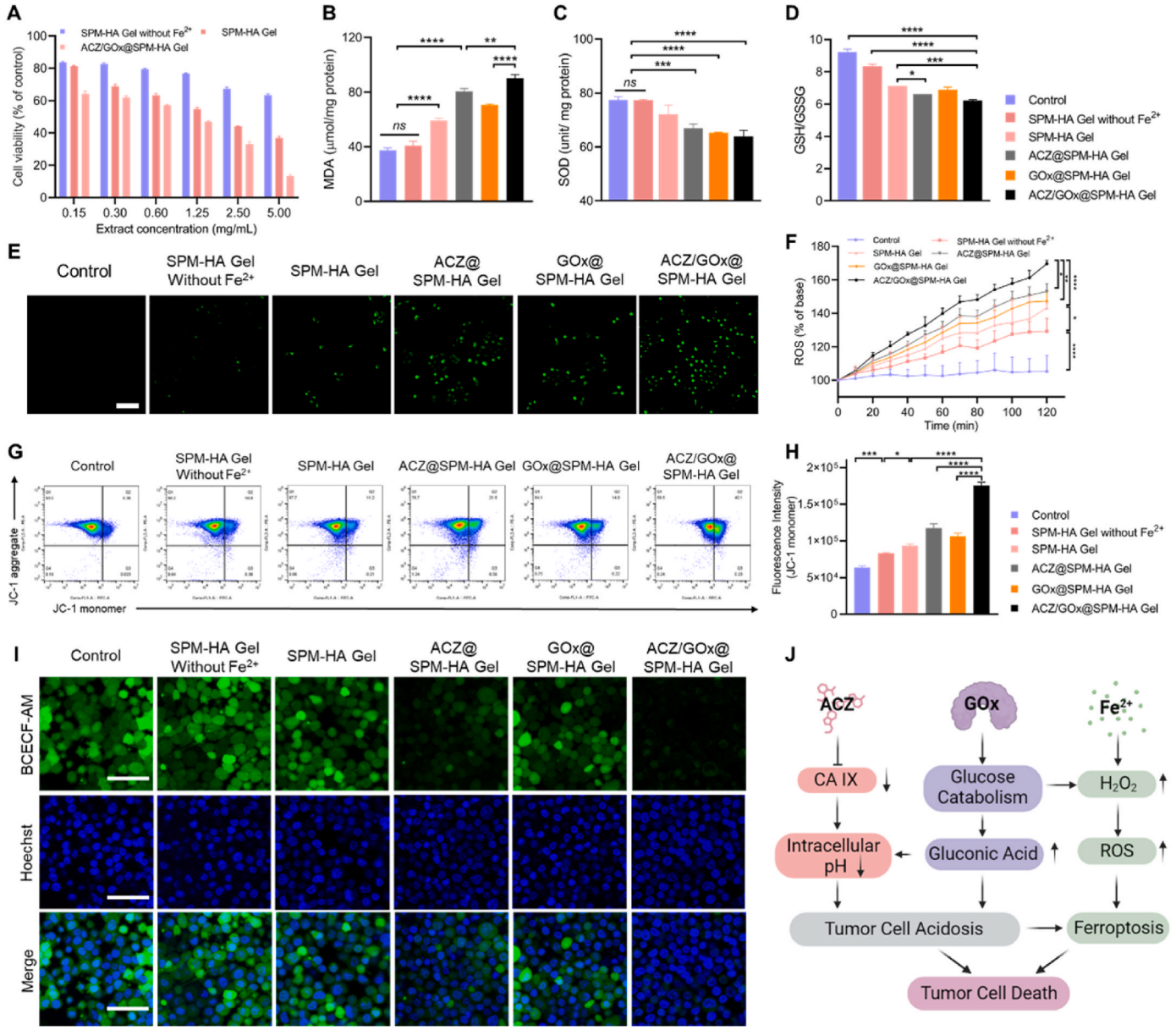

Fig. 3. Cellular oxidative stress induced by ACZ/GOx@SPM-HA Gel. (A) Cell viability of MOC-1 cells after treated with different formulations. (B) MDA, (C) SOD, and (D) GSH/GSSG level in MOC-1 cells after treated with different formulations. (E) Representative fluorescence images of MOC-1 cells stained with DCFH-DA probe after treated with different formulations, scale bar = 100 μm. (F) The plot of intracellular ROS level *vs.* time in 2 h incubation with different formulations. (G) Flow cytometric analysis, and (H) Fluorescence quantitative analysis of mitochondrial membrane potential in MOC-1 cells after treated with different formulations. (I) Representative fluorescence images of intracellular pH of MOC-1 cells stained with BCECF-AM probe after treated with different formulations, scale bar = 50 μm. (J) Schematic illustration of potential anticancer mechanism of ACZ/GOx@SPM-HA Gel. All data are shown as mean ± SD (n = 3).

mechanical property. Therefore, a rotational rheometer was used to investigate the influence of Fe^{2+} coordination on the mechanical properties of SPM-HA Gel according to the protocols described in Supplementary information (Section 1.4). As show in Fig. 2E, without the Fe^{2+}, the gelation time of SPM-DEX and HA-ALD was ~67 s. While with the addition of Fe^{2+}, this time was speeded up for ~50 % (~33 s), indicating the metal ions could further accelerate the chemical crosslinking in the hydrogel scaffold through coordination with abundant hydroxyl groups in SPM-DEX and HA-ALD. As reported by Ghassan H. Matar et al. in their study, imine groups formed from Schiff base reaction may further coordinated with metal ions to further condense the cross-linking framework of hydrogel [50,51]. Therefore, the gelation time of SPM-HA Gel with a series concentration of Fe^{2+} was further evaluate to verify the effect of metal coordination on the cross-linking of this hydrogel. As shown in Fig. S8, with the enhancement of ferrous ions from 0.5 to 2 mg/mL, the gelation time of SPM-HA Gel was significantly reduced from 24.3 s to 15.3 s. Likewise, the release kinetics of ACZ (Fig. S7C) also exhibited a declined tendency with the increasement of Fe^{2+}, verifying the verry essential role of ferrous ions in participating the dynamic chemical cross-linking of SPM-HA Gel. Moreover, owing to this metal coordination in the scaffold, the viscoelasticity of SPM-HA Gel was also significantly enhanced as shown in Fig. 2F. Taken together, SPM-HA Gel with such great self-healing and reversible pH-responsive gelation property holds potency to be translated for the clinical treatment of diseases with different commands.

3.2. Intracellular oxidative stress induced by ACZ/GOx@SPM-HA Gel

Anticancer efficacy of ACZ/GOx@SPM-HA Gel was initially evaluated on MOC-1 cells according to the protocols described in supplementary information (Section 1.5). As shown in Fig. 3A, the cell viability of MOC-1 cells exhibited as dose-dependent manner after incubated with hydrogel extract for 24 h. It should be noted that without the addition of Fe^{2+}, the cell viability of MOC-1 from SPM-HA Gel without Fe^{2+} group could maintain above 80 % at extract concentration up to 0.6 mg/mL, indicating the indispensable role of Fe^{2+} in triggering the ferroptosis. Similar anticancer efficacy on CA-positive cells including A549, MG63, and HEPG2 was also detected by MTT assay (Fig. S9) [52–54]. It should be noted that, though cell viability decreased, NIH3T3 was more tolerant to the treatment of ACZ/GOx@SPM-HA Gel as it expressed lower CA [55]. Therefore, indices representing the cellular redox status were evaluated based the protocols described in supplementary information (Section 1.6). As shown in Fig. 3B-3D, while malondialdehyde (MDA) level from SPM-HA Gel without Fe^{2+} group was comparable to the control group, MDA level from SPM-HA Gel group enhanced for ~57 %, indicating the abnormal lipid peroxidation (LPO) induced by Fe^{2+}. With the addition of ACZ, MDA level was further elevated by 36 % in compare with SPM-HA Gel group. However, the addition of GOx did not significantly enhance the MDA level, considering cells would be tolerable to the glucose catabolism by GOx under the function of carbonic anhydrases IX. The significant increase of MDA level in ACZ/GOx@SPM-HA Gel group proved the above speculation, as the co-treatment of ACZ and GOx could further enhance the MDA level by 11.8 % in compare with ACZ@SPM-HA Gel group. In contrast, opposite trends of SOD level and GSH/GSSG ratio could be observed in Fig. 3C and D, underlying the disturbance of redox homeostasis and the dysfunction of mitochondria. Therefore, oxidative stress in MOC-1 cells was further evaluated. As indicated in Fig. 3E, significant increase of green fluorescence intensity could be observed in cells from ACZ@SPM-HA Gel group, GOx@SPM-HA Gel group, ACZ/GOx@SPM-HA Gel group, suggesting the enhancement of cellular ROS level. Scattered green fluorescence could also detected in SPM-HA Gel group considering the function of Fe^{2+}. Moreover, referred to the change of ROS level in 2 h (Fig. 3F), cellular ROS level in ACZ/GOx@SPM-HA Gel group was elevated for ~61 % in compare with control group, and elevated for 18.3 %, 10.8 %, and 15.1 % in compare with the monotreatment group respectively (SPM-HA Gel group, ACZ@SPM-HA Gel group, and GOx@SPM-HA Gel group). The alternation of mitochondrial membrane potential further confirmed the mitochondrial dysfunction induced by oxidative stress (specific protocols could be referred to the supplementary information (Section 1.7)) as the flow cytometric analysis in Fig. 3G presented an increase trend of JC-1 monomer proportion in all treatment group, especially in ACZ/GOx@SPM-HA Gel group. Quantitative analysis distinctively indicated the significant differences among treatment groups. Specifically, JC-1 monomer fluorescence from ACZ/GOx@SPM-HA Gel group was 87.5 %, 49.7 %, 65.4 % higher than that in monotreatment group respectively. Correspondingly, the oxygen status in MOC-1 cells was assessed using the luminescent oxygen sensor ([Ru(dpp)3]Cl2). As illustrated in Fig. S10, in compare with the control group, the treatment of each formulation decreased the cellular oxygen contents in different extents as the fluorescence intensity of [Ru(dpp)3]Cl2 increased. Specifically, due to the catabolic activity of glucose oxidase (GOx) on glucose within MOC-1 cells, the oxygen levels in both the GOx@SPM-HA Gel group and the ACZ/GOx@SPM-HA Gel group were lower than those in the other treatment groups, consequently decreased the quenching of oxygen on [Ru(dpp)3]Cl2, thereby exhibiting higher fluorescence.

The significant amplification on cellular oxidative stress and mitochondrial dysfunction resulted from the combinative treatment of Fe^{2+}, ACZ and GOx thus intrigued us. To date, ACZ, as an inhibitor of CA, would inhibit its catabolism, retain the intracellular H^+ and consequently lead to cell acidosis, which has been reported as an accelerator for ferroptosis. Therefore, intracellular pH after treated with ACZ/GOx@SPM-HA Gel was investigated by BCECF-AM probe based on the protocols described in supplementary information (Section 1.8). As shown in Fig. 3I, without the ACZ treatment, the green fluorescence intensity from SPM-HA Gel without Fe^{2+} group and SPM-HA Gel group was comparable to the control group (pH = 7.2–7.4). While in ACZ@SPM-HA Gel group, the green fluorescence intensity significantly declined, indicating the decrease of intracellular pH. Though the treatment with GOx@SPM-HA Gel partially decrease the green fluorescence intensity owing to the gluconic acid catalyzed by GOx, the intensity was still distinct. This phenomenon was further confirmed the indispensable role of ACZ in this formulation as the green fluorescence intensity from ACZ/GOx@SPM-HA Gel group was the faintest among all treatment groups.

Taken together, the antitumor mechanism of ACZ/GOx@SPM-HA Gel was deduced as depicted in Fig. 3J. In specific, Fe^{2+}, as the initiator of ferroptosis in this formulation, induces the oxidative stress through Fenton reaction. Meanwhile, under the catabolism of GOx, glucose in the cytoplasm would catalyze into gluconic acid and H_2O_2, which may correspondingly supplement the proton reservoir and H_2O_2 reservoir to fuel cell acidosis and ferroptosis. ACZ, as the CA inhibitor, would block the function of CA IX on maintaining the pH homeostasis and further amplify the cell acidosis and ferroptosis, finally lead to the tumor cell death. Overall, through disrupting the pH and redox homeostasis in cells, ACZ/GOx@SPM-HA Gel holds the antitumor potential to be further evaluated *in vivo*.

3.3. Autophagy-dependent ferroptosis induced by ACZ/GOx@SPM-HA Gel

Accumulating evidence has indicated the interplay between ferroptosis and autophagy at the molecular level through modulating on the ROS generation and the accumulation of iron-dependent LPO. As a mTOR inhibitor, SPM-HA Gel containing spermidine thus holds the potential to amplify the ferroptosis through triggering autophagy in cells. Therefore, with the ferrous ions fixed to 0.2 mg/mL, autophagy and ferroptosis in MOC-1 cells under treatments of series contents of SPM-HA Gel were investigated by CYTO-ID and DHE probes based on the protocols described in supplementary information (Section 1.9). As shown in Fig. 4A and B, green fluorescence representing autophagy

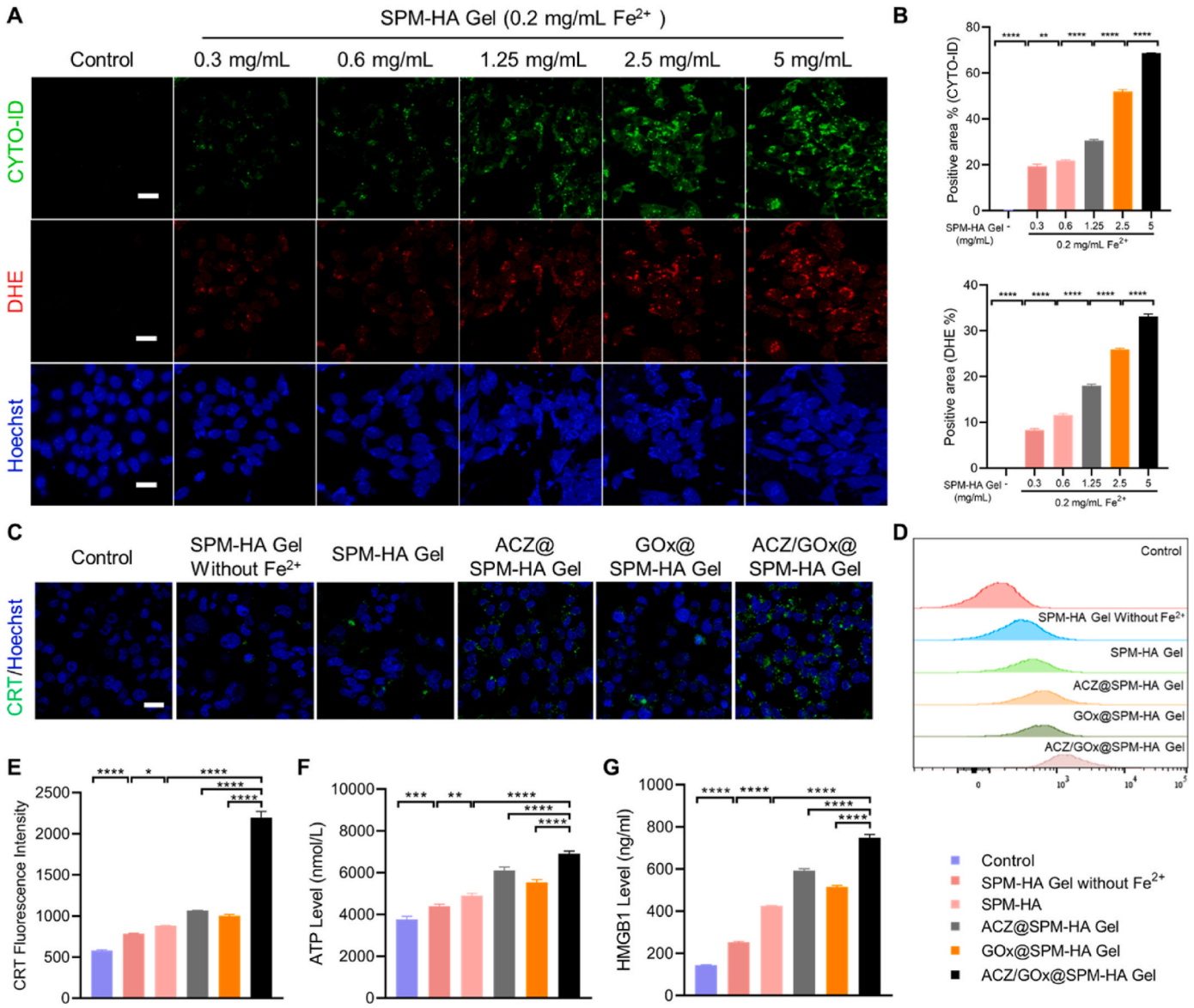

Fig. 4. Autophagy-dependent ferroptosis induced by ACZ/GOx@SPM-HA Gel. (A) Representative fluorescence images of MOC-1 cells stained with CYTO-ID® and DHE probes after treated with different formulations, scale bar = 20 μm. (B) Semiquantitative analysis of autophagy and oxidative stress in cells after treated with different formulations. (C) Representative fluorescence images of MOC-1 cells stained with anti-CRT after treated with different formulations, scale bar = 20 μm. (D)Flow cytometric analysis and (E) Quantitative analysis of CRT expression in MOC-1 cells after treated with different formulations. The level of (F) ATP, and (G) HMGB1 in MOC-1 cells after treated with different formulations. All data are shown as mean ± SD (n = 3).

signal increased in a dose-dependent manner, verifying the physiological function of spermidine. Moreover, though the ferrous ions were fixed, red fluorescence representing the cellular ROS level still increased in a dose-dependent manner, suggesting the effect of autophagy on amplifying ferroptosis in cells. The expressions of two autophagy markers analyzed by western blotting (Fig. S11) further demonstrated the interplay between autophagy and ferroptosis as elevated level of LC3-II and p62 could distinctively be observed with the increase of SPM-DEX concentration while the ferrous ions remained constant.

Ferroptotic cells have been confirmed to release immune stimulative substances *e.g.* damage-associated molecular patterns (DAMPs; calreticulin, ATP, HMGB1) and facilitate the therapy of immune checkpoint blockades. Therefore, cellular calreticulin (CRT) level induced by ACZ/GOx@SPM-HA Gel was studied by flow cytometry and confocal microscopy based on the protocols described in supplementary information (Section 1.10). As observed in Fig. 4C-4E, in compare with the other monotreatment groups, ACZ/GOx@SPM-HA Gel exhibited the strongest fluorescence intensity and was elevated for 1.48-, 1.0-, and 1.1-folds respectively. Similarly, ATP and HMGB1 level in the medium (Fig. 4F and G) also exhibited the same trend, further demonstrating, with the facilitation of autophagy induced by spermidine, ACZ/GOx@SPM-HA Gel may maximally amplify the ferroptosis in cells through disrupting the pH and redox homeostasis. Taken together, ACZ/GOx@SPM-HA Gel may be applicable to be combined with immunotherapy to enhance its response rate and therapeutic outcomes.

3.4. *In vivo antitumor efficacy of ACZ/GOx@SPM-HA Gel*

The antitumor efficacy of ACZ/GOx@SPM-HA Gel was further investigated on MOC-1 tumor bearing mice model as diagram indicated in Fig. 5A. In order to confirm the target of ACZ and anti-PD-L1, the expression of CA IX and PD-L1 in MOC-1 tumor-bearing mice model was firstly evaluated by western blotting analysis. As shown in Fig. S12, high expression levels of both CA IX and PD-L1 expression could be detected

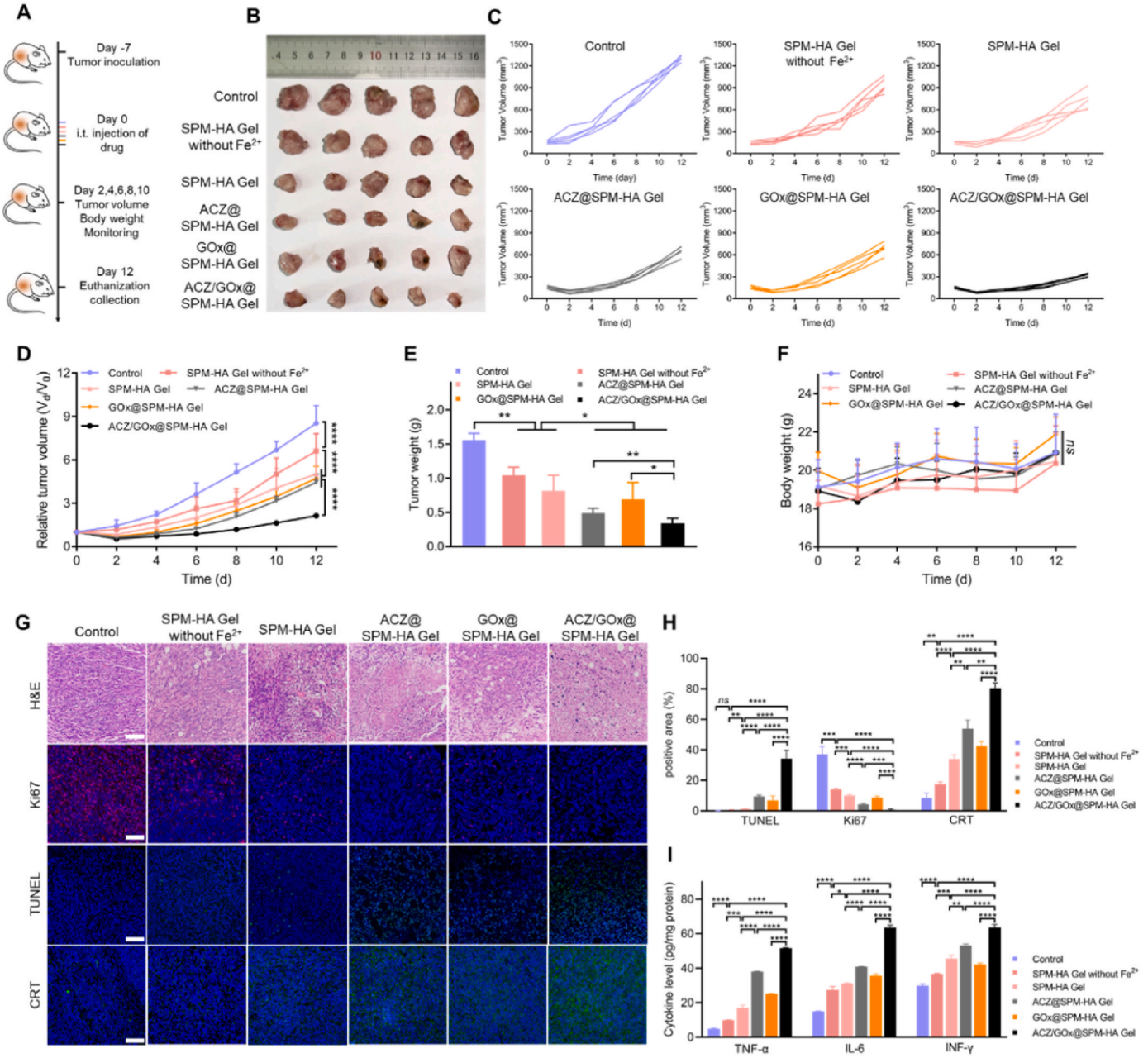

Fig. 5. ***In vivo*** **antitumor efficacy of ACZ/GOx@SPM-HA Gel.** (A) Schematic diagram of antitumor efficacy on MOC-1 tumor-bearing mice model: Whole evaluation lasted for 12 days and different formulations were administered intratumorally on Day 0. (B) Representative photo of resected tumors from each treatment group after 12 days. (C) Tumor volume curves of mice from each treatment group. (D) Relative tumor growth ratio of mice from each treatment group. (E) Weights of resected tumors from each treatment group on Day 12. (F) Body weight of mice from each treatment group during the evaluation. (G) Histological analysis of tumor slices by H&E staining, TUNEL detection, and immunofluorescence staining of Ki67 and CRT, scale bar = 100 μm. (H) Quantitative analysis of the immunofluorescence results. (I) Cytokine levels including TNF-α, IL-6, IFN-γ in mice tumors from each treatment group on Day 12. All data are shown as mean ± SD (n = 5).

in tumor tissues, verifying the feasibility of ACZ/GOx@SPM-HA Gel to be applied in the following *in vivo* experiments. After 12 days evaluation, the growth of resected tumors from each treatment groups (Fig. 5B) were all inhibited in different extents. In specific, as shown in Fig. 5C, while tumor volume from control group sharply climbed to ~1200 mm^3, tumor volume from monotreatment group could be contained at ~600 mm^3. Remarkably, in compare with the uncontrollable and harsh tumor growth in control group, tumor volume from ACZ/GOx@SPM-HA Gel group was decreased for ~75 %. Besides that, tumor volume was further decreased in compare with the monotreatment groups, indicating the great antitumor efficacy of ACZ/GOx@SPM-HA Gel. Relative tumor volume from each treatment group (Fig. 5D) could further demonstrate this conclusion as its relative tumor volume on Day 12 was only elevated for 1.1-fold than that on Day 0. While in control and monotreatment groups, this difference was elevated for 7.5-, 4-, 3.4-, and 3.7-folds respectively. Resected tumor weights (Fig. 5E) also confirmed the above results as tumor weights from ACZ/GOx@SPM-HA Gel group was decreased for 58.3 %, 30.6 %, 50.7 % respectively in compare with monotreatment group. Besides that, mice body weights from all treatment groups (Fig. 5F) fluctuated around 18–21 g, preliminarily suggesting the great biocompatibility and biosafety of ACZ/GOx@SPM-HA Gel. Taken together, it could be concluded the combinative treatment of Fe^{2+}, ACZ and GOx may maximally amplify the effect of SPM-HA Gel on inhibiting the proliferation of MOC-1 xenografts while minimally posing

toxicity to health tissues.

Antitumor efficacy of ACZ/GOx@SPM-HA Gel was further investigated by histological analysis. As shown in Fig. 5G, H&E staining of tumor slices from control group exhibited harsh cancer cell proliferation as purple color zone was nearly covered the whole slice, indicating the active cell division status. In contrast, only scattered purple spots could be observed in tumor slices from ACZ/GOx@SPM-HA Gel group, suggesting the proliferation of MOC-1 cells was inhibited. The further immunofluorescence staining by Ki67 profoundly verified the above observation as the Ki67 positive area (Fig. 5H) from ACZ/GOx@SPM-HA Gel group was decreased for ~98 % in compare with control group. Correspondingly, compared to the control group, the TUNEL signal representing the fragmented DNA in tumor from ACZ/GOx@SPM-HA Gel group significantly increased, demonstrating its great antitumor efficacy. Considering the effect of ferroptosis on inducing immunogenic cell death (ICD), the immune status in tumor tissues was investigated by CRT immunofluorescence staining and ELISA assays of inflammatory cytokines (TNF-α, IL-6, INF-γ). As observed in Fig. 5G and H, in compare with control group, the CRT expression in tumor treated with ACZ/GOx@SPM-HA Gel enhanced for 8.5-folds, confirming the strong effect of ACZ/GOx@SPM-HA Gel on amplifying the ferroptosis in tumor tissues through disrupting the pH and redox homeostasis in an autophagy dependent manner. Moreover, among the monotreatment groups, the CRT expression from ACZ/@SPM-HA Gel group was ~27 % higher than that form GOx@SPM-HA Gel group, underlying the critical role of CA IX inhibitor on alleviating of acidic tumor microenvironment and the immunosuppressive status of infiltrated lymphocytes. The expression of GPX4 and ACSL4 that representing the ferroptosis in tumor tissues was

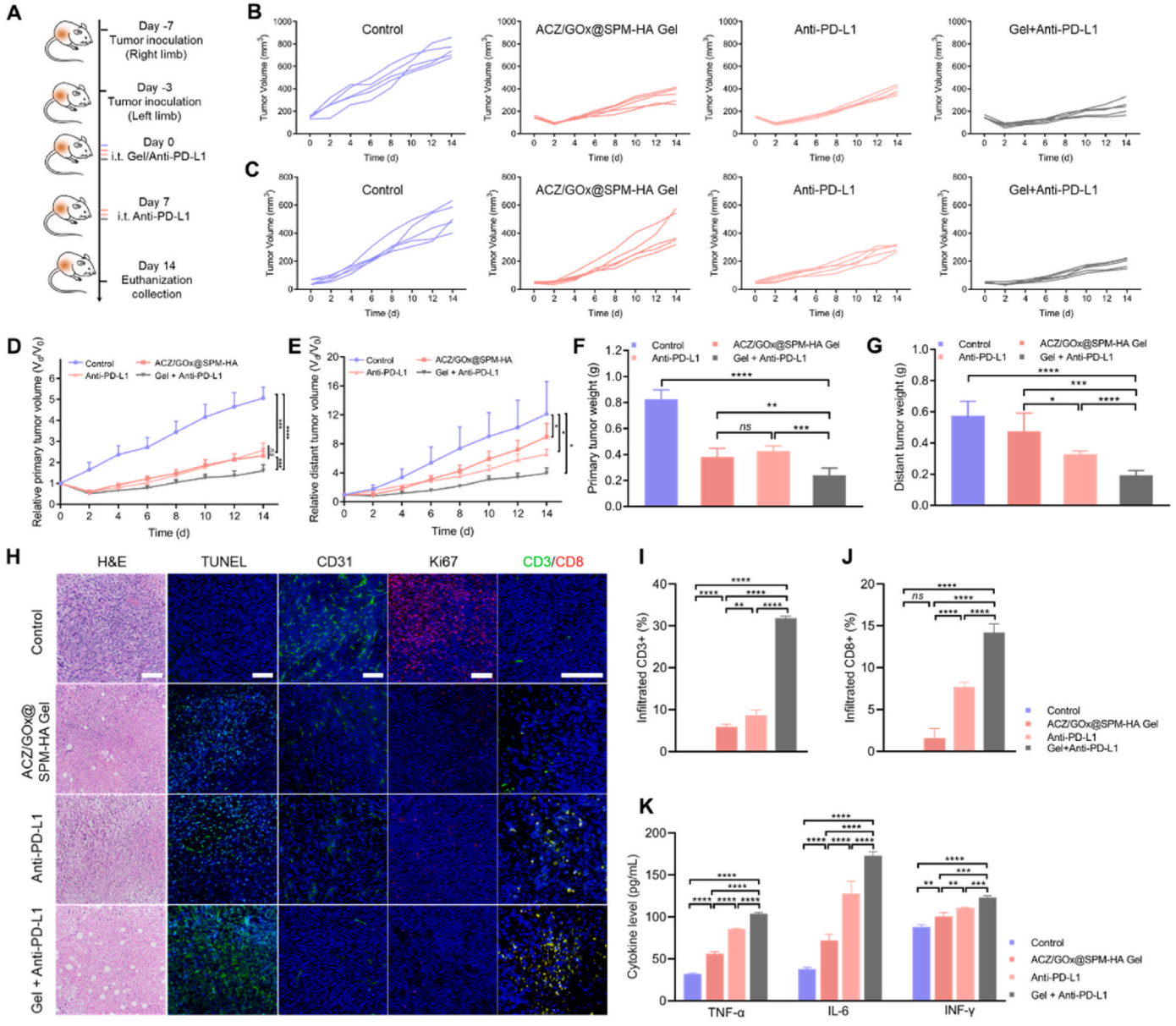

Fig. 6. Anti-metastasis potential of ACZ/GOx@SPM-HA Gel combined with immunotherapy. (A) Schematic diagram of antimetastatic efficacy on MOC-1 tumor-bearing mice metastatic model: Whole evaluation lasted for 14 days and different formulations were administered intratumorally on Day 0 and 7. (B) Primary tumor and (C) Distant tumor volume curves of mice from each treatment group. Relative growth ratio of mice (D) primary tumor and (E) distant tumor from each treatment group. (E) Weights of (F) resected primary tumors and (G) resected distant tumors from each treatment group on Day 14. (H) Histological analysis of distant tumor slices by H&E staining, TUNEL detection, and immunofluorescence staining of Ki67, CD31, and CD3/CD8, scale bar = 100 μm. Quantitative analysis of (I) $CD3^+$ lymphocytes and (J) $CD8^+$ lymphocytes infiltrated in distant tumors. (K) Cytokine levels including TNF-α, IL-6, IFN-γ in mice serum from each treatment group on Day 14. All data are shown as mean ± SD (n = 5).

further verified by western blotting. As Observed in Fig. S13, the expression of GPX4 from ACZ/GOx@SPM-HA Gel group was significantly downregulated, indicating the disturbance of the redox homeostasis in tumor tissues. Correspondingly, the significant up-regulation of ACSL4 could be detected in tumor tissues treated with ACZ/GOx@SPM-HA Gel, demonstrating the participant of ferroptosis in the antitumor mechanism. Cytokine levels in tumor tissues from different treatment groups (Fig. 5I) also verified the above detection. Specifically, in compare with monotreatment groups, TNF-α level from ACZ/GOx@SPM-HA Gel increased for 2-, 0.35-, and 1-fold respectively. Similar trends were also detected in IL-6 and INF-γ, indicating the topical injection of ACZ/GOx@SPM-HA Gel could maximally induce ferroptosis in tumor tissues through the combinative treatment of Fe^{2+}, ACZ and GOx in an autophagy dependent manner.

Taken together, all these data proved the local injection of such hydrogel formulation could efficiently inhibited the tumor growth through ferroptosis induction and distinctively promote the ICD in tumor bed to provide a favorable environment for the therapy of immune checkpoint blockades like PD-L1.

3.5. Combinative immunotherapy with ACZ/GOx@SPM-HA Gel inhibited tumor metastasis

After demonstrating the great antitumor efficacy of ACZ/GOx@SPM-HA Gel on MOC-1 tumor-bearing mice model, its treatment combining with Anti-PD-L1 therapy was further investigated on a MOC-1 tumor-bearing mice metastatic model as depicted in Fig. 6A. After 14 days evaluation, with combinative treatment of ACZ/GOx@SPM-HA Gel and Anti-PD-L1, tumor volume of both primary tumors and distant tumors were significantly decreased. Seen from Fig. 6B and C, it could be noted, in ACZ/GOx@SPM-HA Gel group, though the primary tumor volume could be reduced to ~350 mm^3, its inhibitive effect on the growth of distant tumor was not so obvious (~400 mm^3), indicating the specific antitumor immune response provoked by this hydrogel formulation was not strong enough to prevent the tumor metastasis. In Anti-PD-L1 group, this situation was alleviated as the distant tumor volume could be maintained ~300 mm^3. In contrast, both the primary tumor and distant tumor volume from Gel + Anti-PD-L1 group was maintained around ~200 mm^3, exhibiting great antitumor and antimetastatic effect. The plot of relative tumor volume vs. time (Fig. 6D and E) better presented the tumor growth trend of each treatment group. Specifically, the inhibitive effect of monotreatment by ACZ/GOx@SPM-HA Gel or Anti-PD-L1 on primary tumor growth was comparable as the relative primary tumor volume on Day 14 was both reduced for ~50 % in compare with control group. However, the inhibitive effect between these two monotreatment groups on distant tumors was distinct: in Anti-PD-L1 group, the relative distant tumor volume on Day 14 was 26.7 % lower than that in ACZ/GOx@SPM-HA Gel group, exhibiting better antimetastatic efficacy. Besides that, the combinative treatment of ACZ/GOx@SPM-HA Gel and Anti-PD-L1 significantly decreased the growth of both primary and distant tumors as the relative primary/distant tumor volume on Day 14 was only elevated for 0.6- and 3-fold in compare with Day 0. Correspondingly, in the monotreatment groups, this elevation could be high up to 1.5- and 8-fold. Similar trend was also verified by the primary/distant tumor weight resected form each treatment group (Fig. 6F and G). The body weight change of mice from the combinative treatment group further verified its biosafety as the mice body weights maintained around 21–23 g (Fig. S14).

Histological analysis by H&E staining and immunofluorescence was further performed to better clarify the antitumor and antimetastatic efficacy of the combinative treatment. As shown in Figs. 6H and S15, the positive area of TUNEL signal in distant tumor slices from Gel + Anti-PD-L1 group was high up to ~62 %, which was ~54 % and ~66.7 % higher than that of ACZ/GOx@SPM-HA Gel group and Anti-PD-L1 group respectively. Correspondingly, the positive area of Ki67 signal in distant tumor slices from Gel + Anti-PD-L1 group was only ~0.3 %, suggesting the great antimetastatic efficacy and the robust antitumor immune response induced by the combinative treatment of ACZ/GOx@SPM-HA Gel and immunotherapy. Moreover, CD31 signal, the indicator of angiogenesis, further confirmed the above conclusion as the positive area of CD31 signal in distant tumor slices from Gel + Anti-PD-L1 group was decreased for 76.7 % and 85 % in compare with ACZ/GOx@SPM-HA Gel group and Anti-PD-L1 group respectively. Taken together, local injection of ACZ/GOx@SPM-HA Gel and Anti-PD-L1 could provoke the specific antitumor immune response through triggering the release of DAMPs and thus efficiently inhibit the tumor metastasis.

Therefore, the infiltrated lymphocytes in distant tumors from each treatment groups were investigated by immunofluorescence staining. As observed in Fig. 6H-6I, $CD3^+CD8^+$ lymphocytes could hardly be detected in control group, exhibiting an immunosuppressive microenvironment. While in ACZ/GOx@SPM-HA Gel, though the infiltrated $CD3^+$ lymphocytes proportion could be enhanced to ~6 %, the infiltrated $CD3^+CD8^+$ lymphocytes proportion was only elevated to ~1.5 %. These data thus explained the unsatisfying antimetastatic efficacy of ACZ/GOx@SPM-HA Gel monotreatment as the local injection of such hydrogel formulation was more prone to induce native immune response instead of adaptive immune response through triggering the release of DAMPS and the local inflammation. Intriguingly, in Anti-PD-L1 group, the infiltrated $CD3^+$ lymphocytes proportion (8.6 %) and the infiltrated $CD3^+CD8^+$ lymphocytes proportion (7.7 %) were comparable, indicating the specific antitumor immune response provoked by Anti-PD-L1. Remarkably, in Gel + Anti-PD-L1 group, the infiltrated $CD3^+$ lymphocytes proportion could be high up to 31.8 %, which was elevated for 4.4-, and 2.7-fold in compare with the monotreatment group respectively. Moreover, the infiltrated $CD3^+CD8^+$ lymphocytes proportion was ~85 % higher than that in Anti-PD-L1 group. Serum cytokine levels including TNF-α, IL-6, INF-γ from each treatment group (Fig. 6K) were also consistent with the above analysis. Besides that, the antimetastatic potential of ACZ/GOx@SPM-HA Gel was also verified on a 4T1 orthotopic metastasis model as described in supplementary information (Section 1.12). As shown in Fig. S16, in compare with the malignant lung metastasis in control group, the combinative treatment of ACZ/GOx@SPM-HA Gel and Anti-PD-L1 significantly inhibited the lung metastasis of 4T1 cells. Moreover, in compare with the monotreatment of anti-PD-L1, the tumor nodes in Gel + anti-PD-L1 group was further decreased for ~78 %, demonstrating the antimetastatic efficacy of such combinative treatment. Therefore, it could be concluded that through provoking both native and adaptive immune response, local injection of ACZ/GOx@SPM-HA Gel and Anti-PD-L1 could efficiently inhibited tumor progression and its potential metastasis.

Overall, concluding from the data of xenograft mice model and metastasis mice model, it could be speculated the topical treatment of ACZ/GOx@SPM-HA Gel could maximally induce ferroptosis and ICD in tumor tissues through the combinative treatment of Fe^{2+}, ACZ and GOx in an autophagy dependent manner. Moreover, its integrative treatment with immunotherapy may promote the infiltration of $CD3^+CD8^+$ lymphocytes and provoke both native and adaptive immune response to fight against tumor growth and metastasis, which would be feasible to the multi-mode treatment of HNC.

4. Conclusions

In this study, a self-healable and pH-responsive spermidine hydrogel loaded with ACZ and GOx has been successfully fabricated through the Schiff-base reaction between SPM-DEX and HA-ALD, along with the metal ions (Fe^{2+}) coordination. Investigation on oral squamous cells demonstrated that the ACZ/GOx@SPM-HA Gel may induce cellular oxidative stress and mitochondrial dysfunction through disrupting the pH and redox homeostasis in MOC-1 cells.Moreover, with the facilitation of autophagy induced by spermidine, ACZ/GOx@SPM-HA Gel may maximally amplify the ferroptosis in cells and promote DAMPs release to induce ICD. The results of xenograft mice model and metastasis mice

model further substantiated that the local injection of such hydrogel could efficiently inhibit the tumor growth and distinctively promote the ICD in tumor bed to provide a favorable environment for immunotherapy. Moreover, its integrative treatment with immunotherapy may promote the infiltration of $CD3^+CD8^+$ lymphocytes and provoke both native and adaptive immune response to fight against tumor growth and metastasis. Overall, ACZ/GOx@SPM-HA Gel, with such feasible physiochemical properties and great biocompatibility, holds great potential in treating solid tumors with acidosis-mediated immunotherapy tolerance. However, given that the topical administration of ACZ/GOx@SPM-HA Gel is more likely to elicit innate immune response through promoting the release of DAMPs, it would be more feasible for this hydrogel formulation to be independently applied in the early intervention of tumor while combining it with immunotherapy like anti-PD-L1 in advanced or metastatic stages to achieve better therapeutic outcome.

CRediT authorship contribution statement

Tianqi Nie: Writing – review & editing, Writing – original draft, Methodology, Investigation, Conceptualization. **Yifei Fang:** Writing – review & editing, Visualization, Software, Methodology, Investigation, Data curation. **Ruhe Zhang:** Validation, Methodology, Investigation. **Yishui Cai:** Visualization, Methodology, Formal analysis, Data curation. **Xiaobo Wang:** Validation, Supervision, Formal analysis. **Yuenong Jiao:** Validation, Supervision, Funding acquisition. **Jun Wu:** Writing – review & editing, Validation, Supervision, Funding acquisition.

Data availability statement

The data that support the findings of this study are available on reasonable request from the corresponding authors.

Ethics approval and consent to participate

All the animal experiments were performed in accordance with the guidelines approved by the Institutional Animal Care and Use Committee of Sun Yat-sen University (SYSU-IACUC-2023-000577).

Declaration of competing interest

The authors declare that they have no known competing financial interests or personal relationships that could have appeared to influence the work reported in this paper.

Acknowledgements

This project was supported by the Science and Technology Program of Guangzhou (2024A03J0431 and 2023A03J0488), National Natural Science Foundation of China (52173150 and U22A20315), the Guangzhou Science and Technology Program City-University Joint Funding Project (2024A03J0604), Guangdong Basic and Applied Basic Research Foundation (2023A1515111126). We sincerely acknowledge the funding and generous support from these foundations.

Appendix A. Supplementary data

Supplementary data to this article can be found online at https://doi.org/10.1016/j.bioactmat.2025.01.005.

References

[1] M. He, T. Yang, Y. Wang, et al., Immune checkpoint inhibitor-based strategies for synergistic cancer therapy, Adv. Healthcare Mater. 10 (9) (2021) 2002104.
[2] J. Haanen, M. Ernstoff, Y. Wang, et al., Autoimmune diseases and immune-checkpoint inhibitors for cancer therapy: review of the literature and personalized risk-based prevention strategy, Ann. Oncol. 31 (6) (2020) 724–744.
[3] C. Robert, A decade of immune-checkpoint inhibitors in cancer therapy, Nat. Commun. 11 (1) (2020) 3801.
[4] P. Sharma, S. Goswami, D. Raychaudhuri, et al., Immune checkpoint therapy—current perspectives and future directions, Cell 186 (8) (2023) 1652–1669.
[5] E.C. Scott, A.C. Baines, Y. Gong, et al., Trends in the approval of cancer therapies by the FDA in the twenty-first century, Nat. Rev. Drug Discov. 22 (8) (2023) 625–640.
[6] M. Ramos-Casals, J.R. Brahmer, M.K. Callahan, et al., Immune-related adverse events of checkpoint inhibitors, Nat. Rev. Dis. Prim. 6 (1) (2020) 38.
[7] E. Ghisoni, A. Wicky, H. Bouchaab, et al., Late-onset and long-lasting immune-related adverse events from immune checkpoint-inhibitors: an overlooked aspect in immunotherapy, Eur. J. Cancer 149 (2021) 153–164.
[8] Q. Yin, L. Wu, L. Han, et al., Immune-related adverse events of immune checkpoint inhibitors: a review, Front. Immunol. 14 (2023) 1167975.
[9] J. Li, F. Cao, H.-l Yin, et al., Ferroptosis: past, present and future, Cell Death Dis. 11 (2) (2020) 88.
[10] D. Tang, G. Kroemer, R. Kang, Ferroptosis in immunostimulation and immunosuppression, Immunol. Rev. 321 (1) (2024) 199–210.
[11] D. Tang, G. Kroemer, Ferroptosis, Curr. Biol. 30 (21) (2020) R1292–R1297.
[12] S. Doll, B. Proneth, Y.Y. Tyurina, et al., A. ACSL4 dictates ferroptosis sensitivity by shaping cellular lipid composition, Nat. Chem. Biol. 13 (1) (2017) 91–98.
[13] C.W. Brown, J.J. Amante, P. Chhoy, et al., Prominin2 drives ferroptosis resistance by stimulating iron export, Dev. Cell 51 (5) (2019) 575–586, e574.
[14] Y. Wang, L. Zheng, W. Shang, et al., Wnt/beta-catenin signaling confers ferroptosis resistance by targeting GPX4 in gastric cancer, Cell Death Differ. 29 (11) (2022) 2190–2202.
[15] X. Jiang, B.R. Stockwell, M. Conrad, et al., Ferroptosis: mechanisms, biology and role in disease, Nat. Rev. Mol. Cell Biol. 22 (4) (2021) 266–282.
[16] C. Corbet, O. Feron, Tumour acidosis: from the passenger to the driver's seat, Nat. Rev. Cancer 17 (10) (2017) 577–593.
[17] X. Chen, H. Zhang, M. Zhang, et al., Amorphous Fe-based nanoagents for self-enhanced chemodynamic therapy by re-establishing tumor acidosis, Adv. Funct. Mater. 30 (6) (2020) 1908365.
[18] C. Michiels, C. Tellier, O. Feron, Cycling hypoxia: a key feature of the tumor microenvironment, Biochim. Biophys. Acta (BBA)-Rev. Cancer 1866 (1) (2016) 76–86.
[19] D. Neri, C.T. Supuran, Interfering with pH regulation in tumours as a therapeutic strategy, Nat. Rev. Drug Discov. 10 (10) (2011) 767–777.
[20] L. Pisarsky, R. Bill, E. Fagiani, et al., Targeting metabolic symbiosis to overcome resistance to anti-angiogenic therapy, Cell Rep. 15 (6) (2016) 1161–1174.
[21] J.R. Doherty, J.L. Cleveland, Targeting lactate metabolism for cancer therapeutics, J. Clin. Invest. 123 (9) (2013) 3685–3692.
[22] I. Marchiq, J. Pouysségur, Hypoxia, cancer metabolism and the therapeutic benefit of targeting lactate/H+ symporters, J. Mol. Med. 94 (2016) 155–171.
[23] L. Schwartz, T. Seyfried, K.O. Alfarouk, Out of Warburg effect: an effective cancer treatment targeting the tumor specific metabolism and dysregulated pH, Semin. Cancer Biol. 43 (2017) 134–138.
[24] S. Pastorekova, R.J. Gillies, The role of carbonic anhydrase IX in cancer development: links to hypoxia, acidosis, and beyond, Cancer Metastasis Rev. 38 (2019) 65–77.
[25] H.M. Becker, Carbonic anhydrase IX and acid transport in cancer, Br. J. Cancer 122 (2) (2020) 157–167.
[26] M. Swayampakula, P. McDonald, M. Vallejo, et al., The interactome of metabolic enzyme carbonic anhydrase IX reveals novel roles in tumor cell migration and invadopodia/MMP14-mediated invasion, Oncogene 36 (45) (2017) 6244–6261.
[27] S.C. Chafe, Y. Lou, J. Sceneay, et al., Carbonic anhydrase IX promotes myeloid-derived suppressor cell mobilization and establishment of a metastatic niche by stimulating G-CSF production, Cancer Res. 75 (6) (2015) 996–1008.
[28] H.S. Jung, J. Han, H. Shi, et al., Overcoming the limits of hypoxia in photodynamic therapy: a carbonic anhydrase IX-targeted approach, J. Am. Chem. Soc. 139 (22) (2017) 7595–7602.
[29] A. Brand, K. Singer, G.E. Koehl, et al., LDHA-associated lactic acid production blunts tumor immunosurveillance by T and NK cells, Cell Metabol. 24 (5) (2016) 657–671.
[30] M.J. Watson, P.D. Vignali, S.J. Mullett, et al., Metabolic support of tumour-infiltrating regulatory T cells by lactic acid, Nature 591 (7851) (2021) 645–651.
[31] S.C. Chafe, F.S. Vizeacoumar, G. Venkateswaran, et al., Genome-wide synthetic lethal screen unveils novel CAIX-NFS1/xCT axis as a targetable vulnerability in hypoxic solid tumors, Sci. Adv. 7 (35) (2021) eabj0364.
[32] A.C. Kimmelman, E. White, Autophagy and tumor metabolism, Cell Metabol. 25 (5) (2017) 1037–1043.
[33] E.E. Mowers, M.N. Sharifi, K.F. Macleod, Functions of autophagy in the tumor microenvironment and cancer metastasis, FEBS J. 285 (10) (2018) 1751–1766.
[34] J. Debnath, N. Gammoh, K.M. Ryan, Autophagy and autophagy-related pathways in cancer, Nat. Rev. Mol. Cell Biol. 24 (8) (2023) 560–575.
[35] W. Gao, X. Wang, Y. Zhou, et al., Autophagy, ferroptosis, pyroptosis, and necroptosis in tumor immunotherapy, Signal Transduct. Targeted Ther. 7 (1) (2022) 196.
[36] B. Zhou, J. Liu, R. Kang, et al., Ferroptosis is a type of autophagy-dependent cell death, Semin. Cancer Biol. 66 (2020) 89–100.
[37] S. Lee, N. Hwang, B.G. Seok, et al., Autophagy mediates an amplification loop during ferroptosis, Cell Death Dis. 14 (7) (2023) 464.
[38] J. Li, J. Liu, Y. Xu, et al., Tumor heterogeneity in autophagy-dependent ferroptosis, Autophagy 17 (11) (2021) 3361–3374.

[39] E. Dai, L. Han, J. Liu, et al., Autophagy-dependent ferroptosis drives tumor-associated macrophage polarization via release and uptake of oncogenic KRAS protein, Autophagy 16 (11) (2020) 2069–2083.
[40] Z. Zhang, Z. Yao, L. Wang, et al., Activation of ferritinophagy is required for the RNA-binding protein ELAVL1/HuR to regulate ferroptosis in hepatic stellate cells, Autophagy 14 (12) (2018) 2083–2103.
[41] T. Nie, H. Liu, Z. Fang, et al., Tumor microenvironment mediated spermidine-metal-immunopeptide nanocomplex for boosting ferroptotic immunotherapy of lymphoma, ACS Nano 17 (11) (2023) 10925–10937.
[42] N. Kong, H. Zhang, C. Feng, et al., Arsenene-mediated multiple independently targeted reactive oxygen species burst for cancer therapy, Nat. Commun. 12 (1) (2021) 4777.
[43] J.-L. Liang, X.-K. Jin, G.-F. Luo, et al., Immunostimulant hydrogel-guided tumor microenvironment reprogramming to efficiently potentiate macrophage-mediated cellular phagocytosis for systemic cancer immunotherapy, ACS Nano 17 (17) (2023) 17217–17232.
[44] Z. Guo, J. Zhou, Y. Yu, et al., Immunostimulatory DNA hydrogel enhances protective efficacy of nanotoxoids against bacterial infection, Adv. Mater. 35 (31) (2023) 2211717.
[45] Y. Fang, T. Nie, G. Li, et al., Multifunctional antibiotic hydrogel doped with antioxidative lycopene-based liposome for accelerative diabetic wound healing, Chem. Eng. J. 480 (2024) 147930.
[46] T. Chanmee, P. Ontong, N. Itano, et al., Hyaluronan: a modulator of the tumor microenvironment, Cancer Lett. 375 (1) (2016) 20–30.
[47] A. Devi Vk, R. Shyam, A. Palaniappan, et al., Self-healing hydrogels: preparation, mechanism and advancement in biomedical applications, Poplymers 13 (21) (2021) 3782.
[48] S. Srivastav, A. Singh, M.P. Singh, et al., Injectable self-healing hydrogel as a rising therapeutic strategy for the locoregional management of cancer, J. Drug Deliv. Sci. Technol. (2024) 105913.
[49] B.N. Kharbikar, P. Mohindra, T.A. Desai, Biomaterials to enhance stem cell transplantation, Cell Stem Cell 29 (5) (2022) 692–721.
[50] G.H. Matar, E. Kaymazlar, M. Andac, et al., Novel binary blended hydrogel films (Chitosan-Vanillin Schiff base/locust bean gum and Fe (III), Cu (II) & Zn (II) complexes): Synthesis, characterization, conductivity, and antibacterial acivivity, J. Polym. Environ. 31 (8) (2023) 3509–3521.
[51] M.T. Kaczmarek, T. Malogorzata M. Nowak, et al., Lanthanides: Schiff base complexes, applications in cancer diagnosis, therapy, and antibacterial acivity, Coord. Chem. Rev. 379 (2018) 42–54.
[52] M. Ilie, V. Hofman, J. Zangari, et al., Response of CAIX and CAXII to in vitro re-oxygenation and clinical significance of the combined expression in NSCLC patients, Lung Cancer 82 (1) (2013) 16–23.
[53] F. Perut, F. Carta, G. Bonuccelli, et al., Carbonic anhydrase IX inhibition is an effective strategy for esteosarcoma treatment, Expert Opin. Ther. Targets 19 (12) (2015) 1593–1605.
[54] S.J. Yu, J.H. Yoon, J.H. Lee, et al., Inhibition of hypoxia-inducible carbonic anhydrase-IX enhances hexokinase II inhibitor-induced hepatocellular carcinoma cell apoptosis, Acta Pharmacol. Sin. 32 (7) (2011) 912–920.
[55] M. Takacova, M. Barathova, M. Zatovicova, et al., Carbonic anhydrase IX-mouse versus human, Int. J. Mol. Sci. 21 (1) (2019) 246.